Check for updates

Eco-inspired synthesis of MgO-infused g-C₃N₄ nanocomposites from tulsi seeds for advanced photocatalytic environmental remediation†

Sweety Dahiya,[a] Anshu Sharma[b] and Sudesh Chaudhary ⓘ *[a]

This study introduces a novel approach to synthesizing magnesium oxide (MgO) nanoparticles through the use of *Ocimum sanctum* (tulsi seed) extract combined with the thermal polymerization of MgO-doped graphitic carbon nitride (MgCN) nanocomposites. The nanocomposites were prepared at varying MgO concentrations (0.5 mM, 1.0 mM, 1.5 mM, and 2.0 mM) to optimize their properties. Comprehensive characterization of the synthesized MgO nanoparticles and MgCN nanocomposites was conducted using advanced analytical techniques, including UV-Vis spectroscopy, X-ray diffraction (XRD), scanning electron microscopy with energy dispersive X-ray mapping (SEM-EDX), Fourier-transform infrared spectroscopy (FTIR), and thermogravimetric analysis (TGA). The MgCN nanocomposite with 1.5 mM MgO demonstrated a high surface area of 98.287 m^2 g^{-1}, as determined by Brunauer–Emmett–Teller (BET) analysis. X-ray photoelectron spectroscopy (XPS) confirmed the presence of carbon and nitrogen elements, validating the integration of MgO into the nanocomposite matrix. High-resolution transmission electron microscopy (HRTEM) images depicted planar, stacked, and wrinkled structures characteristic of a graphitic-like material. Consistent with a Z-scheme heterojunction, the MgCN (1.5 mM) sample exhibited an enhanced morphology, increased surface area, improved visible light absorption, and reduced band gap. This particular nanocomposite displayed remarkable adsorption and photocatalytic degradation capabilities, achieving up to 98% removal of methylene blue and 54% removal of tetracycline antibiotics. Furthermore, it showed significant antibacterial activity against *Escherichia coli*. Notably, the MgCN (1.5 mM) nanocomposite maintained its performance over four cycles, underscoring its potential for sustained application in wastewater treatment and the elimination of organic contaminants. The scavenging activity of the nanocomposites was also explored, revealing additional environmental benefits. This research highlights a promising pathway for developing eco-friendly nanocomposites with robust capabilities in water purification and pollution control.

1. Introduction

The accumulation of contaminants in the water system has emerged as one of the environmental issues that protective entities must handle. Antibiotics are the primary class of pharmaceuticals among the numerous developing pollutants found in a variety of water matrices.[1] Numerous studies have demonstrated that both people and animals have poor digestion of a wide range of antibiotics. Several sources, including wastewater from hospitals, the pharmaceutical industry, the textile industries, and animal and human waste dumps, are the routes by which these antibiotics enter water bodies and the environment.[2] Due to extreme persistence and toxicity to aquatic life, they are of great concern as they contaminate the environment, particularly soil and water bodies. One of the most used antibiotics for treating infections in humans is tetracycline.[3] According to multiple investigations, within two hours of consumption, more than 60% of tetracycline given orally to humans is eliminated by urine.[4] At the moment, reports of tetracycline concentrations in home, industrial, and hospital wastewater vary from ng L^{-1} to mg L^{-1}. Various methods, including adsorption, sophisticated oxidation procedures, and membrane filtering, have been employed to eliminate antibiotics from various media.[5] Advanced oxidation processes (AOPs)[6] have been proven to be the most successful method for removing these medications when combined with other procedures.[7] With the ability to function in ambient circumstances and use sunlight as a source of energy, this

[a] *Centre of Excellence for Energy and Environmental Studies, Deenbandhu Chhotu Ram University of Science and Technology, Murthal, Sonipat 131039, Haryana, India. E-mail: sudesh.energy@dcrustm.org, anshushsharda@gmail.com*

[b] *Department of Physics under School of Engineering and Technology, Central University of Haryana, Mahendergarh 123031, Haryana, India*

† Electronic supplementary information (ESI) available. See DOI: https://doi.org/10.1039/d4cp03673e

technology uses hydroxyl radicals to convert organic molecules into innocuous chemicals.[8] Photocatalysis is an emerging AOP technology that uses nanoscale catalysts and light to activate chemical processes. Exploring sustainable and efficient materials for environmental remediation and energy conversion is a key area of interest in modern materials science.[9] With its exceptional electronic properties, chemical stability, and non-toxic nature, graphitic carbon nitride has become a highly intriguing nanomaterial. Its photocatalytic capabilities, including the removal of pollutants and the harvesting of solar energy, render it a promising material for such endeavours.[10] Nevertheless, g-C_3N_4 has certain limitations, such as a low surface area and a limited range of light absorption, which require modifications to enhance its performance.[11] One potential method for augmenting the characteristics of g-C_3N_4 involves the introduction of metal oxides via doping, such as magnesium oxide (MgO). In contrast, the photocatalytic activity of pristine g-C_3N_4 is significantly impeded by the rapid recombination rates and small surface area of the photogenerated charge carriers.[12] To mitigate the rate of charge carrier recombination, g-C_3N_4 endured doping with sensitizers, metal, and non-metal elements.[13] The underlying objective is to fabricate a heterojunction capable of transporting charge carriers across interfaces while reducing their recombination rate. Numerous semiconducting substances, including TiO_2, NiO, ZnO, SiO_2, and Al_2O_3, have been incorporated into g-C_3N_4 supports to produce these types of heterojunction.[14] In an effort to produce hybrid g-C_3N_4, which has similar applications to water splitting and efficient fuel conversion from CO_2, numerous low-dimensional carbonaceous materials,[15] including graphene,[16] transition metal chalcogenides, carbon nanotubes and carbon dots, recently underwent significant development in terms of their physical properties (Paul et al., 2021).[17]

By enhancing the bandgap and charge separation efficiency, the photocatalytic activity can be significantly improved. In addition, the synthesis method is crucial in determining the structural and functional attributes of the resulting nanocomposites.[18] Traditional synthesis techniques frequently employ corrosive reagents and severe environments, which runs counter to the objective of sustainability.[19]

In response to the aforementioned obstacles, the current investigation presents a novel and environmentally sustainable methodology for producing g-C_3N_4 nanocomposites doped with MgO, employing tulsi seeds (Ocimum sanctum) as a natural precursor. Prominent bioactive compounds found in tulsi seeds, scientifically referred to as Ocimum tenuiflorum, include flavonoids and phenolic acids.[20] These compounds have demonstrated remarkable potential as capping and reducing agents. Tulsi (Ocimum sanctum), commonly known as holy basil, is highly regarded in traditional medicine for its numerous health benefits. The seeds of tulsi are particularly rich in bioactive compounds, including polyphenols and flavonoids, which are known for their potent antioxidant, anti-inflammatory, and antimicrobial properties. Research has demonstrated that these phytochemicals can effectively scavenge free radicals, thus mitigating oxidative stress and promoting overall health. This naturally-derived approach to nanoparticle production not only enhances

their biocompatibility but also positions them favorably for environmental and biomedical applications. Moreover, the utility of tulsi seed extracts is expanding beyond medicinal applications; they are being investigated for their role in sustainable materials science. The synergistic effects of tulsi extracts when combined with other natural substances could lead to the development of groundbreaking eco-friendly materials with applications in catalysis and drug delivery. Utilizing tulsi seeds in green synthesis offers numerous benefits compared to traditional chemical synthesis methods.[21] For starters, environmentally sustainable green synthesis techniques employing tulsi seeds are cost-effective and necessitate a comparatively modest amount of energy to commence the reaction.[22] Additionally, it is worth noting that tulsi seeds comprise a diverse array of phytochemicals, including amides, flavones, carboxylic acids, phenols, ascorbic acids, and ketones, all of which possess the ability to reduce metal ions into metal nanoparticles.[23] Stability is imparted to the synthesized nanoparticles by the reducing and capping actions of these phytochemicals.[24] Additionally, research has demonstrated that tulsi seeds possess robust antioxidant and anti-inflammatory properties, which may be infused into the nanoparticles that are synthesized. Owing to these properties, tulsi seed-derived nanoparticles can be used in a variety of applications, including optical imaging, molecular sensing, catalysis, antimicrobials, biomedical diagnostics, and biological system labelling.[25]

This study seeks to assess the photocatalytic capabilities of the MgO-doped g-C_3N_4 nanocomposites created through an environmentally friendly approach involving tulsi seeds. The efficiency of photocatalysis is evaluated by studying the breakdown of organic pollutants when exposed to visible light. The synthesized nanocomposites undergo thorough characterization using a range of analytical techniques. Scanning electron microscopy (SEM), X-ray diffraction (XRD), transmission electron microscopy (TEM), and UV-vis diffuse reflectance spectroscopy are among the following. These techniques enable the analysis of the structural, morphological, and optical characteristics of the nanocomposites.

The results obtained from this research have the potential to significantly contribute to the field of photocatalysis by providing a sustainable and effective method for producing g-C_3N_4 nanocomposites doped with MgO. The innovative utilization of tulsi seeds not only aligns with the principles of green chemistry but also opens up possibilities for investigating the potential of bio-based precursors in nanomaterial synthesis. This investigation enhances the collective comprehension of sustainable materials science and its practical implementations within the domains of energy and the environment.

2. Experimental section

2.1 Materials and glassware

Commercially accessible reagents were used in the synthesis of the samples; none of these reagents underwent further purification or processing prior to use. The primary precursors employed in this study were urea with a purity of 99.99% and

This journal is © the Owner Societies 2024

Phys. Chem. Chem. Phys., 2024, **26**, 28064–28081 | **28065**

high-purity magnesium acetate obtained from Thermo Fisher Scientific. The seeds of tulsi (*Ocimum sanctum*) were collected in the vicinity of DCRUST, Murthal, Haryana (India). The experimental glassware employed in the study was made from borosilicate glass, which is renowned for its exceptional chemical resistance and long-lasting nature. A comprehensive decontamination procedure was implemented prior to the use of the glassware, which involved submerging it in a 10% nitric acid solution for a duration of 18 hours. The glassware was kept in perfect conditions for the experiments by rinsing it with double-distilled water after the acid bath to get rid of any remaining acid and then washing it with ordinary water.

2.2 Preparation of tulsi seed extract (TSE)

In order to eradicate any remaining soil and particulate impurities, a total of two infusions with tap water and one infusion with deionized water were performed on 30 grams of desiccated tulsi (*Ocimum sanctum*) seeds.[26] Subsequently, 40 mL of deionized water was added to the cleansed seeds in a 500 mL borosilicate beaker (see Fig. 1). The mixture was heated to 70 °C and kept at this temperature until the aqueous solution acquired a noticeable, deep brown color, indicating successful extraction. Once the desired color was achieved, the mixture was cooled, and the liquid was carefully separated and filtered using Whatman filter paper to eliminate any remaining impurities. The filtrate (TSE) was then kept at 4 °C until needed in the synthesis procedure.

2.3 Synthesis of MgO nanoparticles

A 1 mM solution of magnesium nitrate hexahydrate underwent stirring with 40 mL of distilled water. Until a clear solution was achieved, the mixture was agitated using a magnetic stirrer. Subsequently, 20 mL of the tulsi seed extract was incrementally introduced to the molar solution at consistent intervals of 2 to 3 minutes, one drop at a time. The solution was continuously swirled for approximately four hours.[27] After the continuous stirring, periodically washing the precipitates with acetone and distilled water, they were centrifuged for 15 minutes at 5000 rpm and then kept to dry in the oven for 8 h at 80 °C

(Fig. 2). The completely dried sample was then transferred to a crucible and it was kept for calcination for about 4 hours at 450 °C.[28] At the end of this procedure, white-coloured MgO NPs were obtained.

Overall process:

1. Reduction and stabilization:

● The phytochemicals present in tulsi extract, such as polyphenols, flavonoids, and other compounds, act to reduce the magnesium ions Mg^{2+} to magnesium oxide nanoparticles MgO.

2. Formation of nanoparticles:

● During the reaction, the magnesium ions undergo nucleation and grow into nanoparticles, while the phytoconstituents help stabilize the nanoparticles, preventing agglomeration.

$$Mg^{2+} \text{ (metal salts)} + \text{polyphenols (plant extracts)} \rightarrow Mg^0$$

2.4 Synthesis of g-C₃N₄

10 g of urea was dissolved in 10 mL of distilled water at 30 °C while being constantly stirred in order to yield graphitic carbon nitride (g-C_3N_4). The solution that resulted was subsequently heated in a hot air furnace at 110 °C for one hour.[29] After that, the powder was heated in a muffle furnace at 550 °C for three hours, with a heating rate of 2 °C per minute. The thermal process effectively compressed the powder in a porcelain crucible and prevented the escape of gas. By carefully grinding the product in a mortar and pestle, a pure, finely powdered g-C_3N_4 was obtained.[30]

2.5 Fabrication of nanocomposites

For the synthesis of MgO-modified graphitic carbon nitride (GCN), a mixture was formed by combining 10 g of urea with different concentrations of magnesium oxide nanoparticles (MgO-NPs) in an aqueous suspension. Concentrations of 0.5 mM, 1.0 mM, 1.5 mM, and 2.0 mM were mixed with 50 mL of distilled water in four separate beakers labelled A, B, C, and D, respectively, following standard laboratory procedures. A magnetic stirrer was employed to implement continuous agitation of the mixtures. Afterward, 20 mL of tulsi seed extract
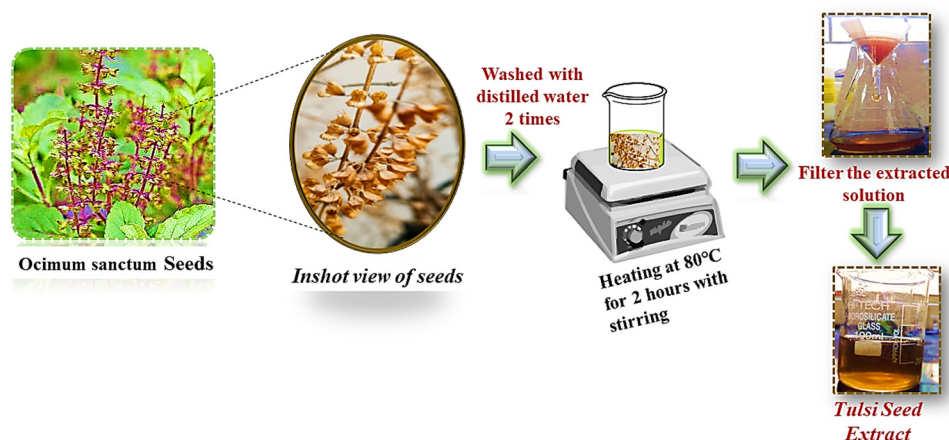

Fig. 1 Preparation of tulsi seed (*Ocimum sanctum*) extract (TSE).

28066 | *Phys. Chem. Chem. Phys.*, 2024, **26**, 28064–28081

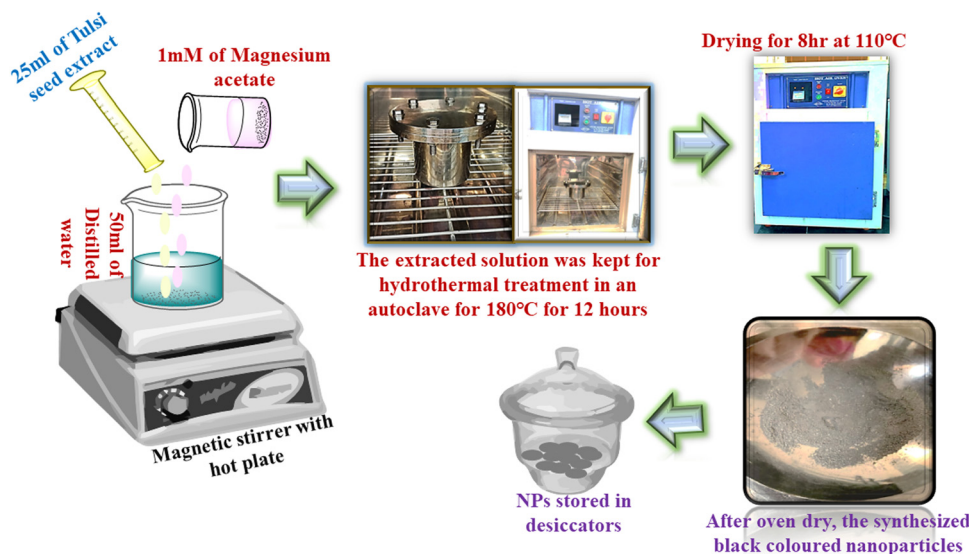This journal is © the Owner Societies 2024

Fig. 2 Synthesis of MgO NPs using TSE.

was carefully added drop by drop to each of the four beakers at regular intervals (Dahiya *et al.*, 2023). The TSE caused a clear shift in colour in each suspension, suggesting different concentrations of MgO-NPs. At a concentration of 0.5 mM, the solution displayed a greenish-yellow colour. Increasing the concentration to 1.0 mM, 1.5 mM, and 2.0 mM resulted in progressively darker shades of yellow, ranging from greenish-dark yellow to yellow and finally dark yellow. The mixtures were stirred consistently for a period of 2 hours to foster the development of precipitates.[31] The samples underwent a 15-minute centrifugation at 5000 rpm to separate and purify the precipitates subsequent to a thorough washing with acetone and distilled water along with a stirring procedure, as shown in Fig. 3. The purified precipitates were then dried in a hot air oven at 80 °C for about 8 hours.[32] The drying process was then followed by calcination of the dried precipitates at 450 °C for

4 hours, resulting in the formation of unique color variations across the different concentrations: raven black for 0.5 mM, charcoal black for 1.0 mM, coal-black for 1.5 mM, and jet black for 2.0 mM. In order to maintain the integrity of the samples for subsequent experimental uses, they were ultimately sealed in hermetic containers. The synthesis of MgO-modified g-C_3N_4 nanocomposites (named MgCN nanocomposites) with customized properties for prospective photocatalytic activities was accomplished in a refined and regulated manner using this protocol.

2.6 Antibacterial methodology

Using the agar well diffusion method, the antibacterial activity of the phytoextract route synthesized MgCN nanocomposites against *Escherichia coli* has been evaluated. The bacterial growth took place on the nutrient agar medium. Following

Fig. 3 Fabrication of MgO doped g-C_3N_4 nanocomposites (MgCN) at varying conc.

This journal is © the Owner Societies 2024

Phys. Chem. Chem. Phys., 2024, **26**, 28064–28081 | **28067**

this, using a sterile cotton swab to solidify, this mixture gets spread over the Petri plates, and new bacterial cultures are dispensed across the plates. Using a cork borer, the wells were punched onto the agar plates and filled with varying concentrations of the stock solution, starting at 200 μg mL^{-1}.[33] Following this, the plates were kept at 37 °C for a full day, during which time the inhibition zones surrounding the well were monitored. By measuring the inhibition zone's circumference in millimeters around the well, the zone of inhibition was determined.[34]

2.7 Qualitative phytochemical screening

The identification of diverse phytoconstituents in the tulsi seed extract was conducted employing standardized phytochemical methodologies[35]

3. Structural and morphological analysis

A variety of analytical procedures were used to characterize MgO NPs, g-C$_3$N$_4$, and MgCN NCs synthesized using the phytoextract approach. Utilizing X-ray diffraction with a Bruker D8 diffractometer and Cu Kα radiation (λ = 1.5418) across the 2θ = 20–80° range, the crystallized phases of MgO NPs, g-C$_3$N$_4$, and MgCN nanocomposites were analyzed. The Fourier transform infrared spectra (FTIR) of the samples was acquired throughout the range of 500–4000 cm^{-1} using a PerkinElmer spectrometer. Under the wavelength range of 400–800 nanometers, ultraviolet-visible (UV-Vis) diffuse reflection spectra were acquired using a Shimadzu UV-2600 I UV-Vis spectrophotometer. Transmission electron microscopy (TEM) using a Talos F200X microscope and scanning electron microscopy (SEM) employing a JSM 7900-F microscope were employed to perform comprehensive structural and morphological characterization. An experiment was conducted using a PerkinElmer 4000 system to perform thermogravimetric analysis (TGA). XPS was also done to check the purity and chemical composition of the prepared nanocomposites. During the analysis, the sample was heated from room temperature to 800 °C at a rate of 10 °C min^{-1} in an N$_2$ atmosphere.

4. Photocatalytic activity

By tracking the photocatalytic degradation of the dye methylene blue and antibiotic in aqueous solutions, the photocatalytic activity of the synthesized compounds was assessed. To simulate solar irradiation, photocatalytic experiments were conducted in a specially designed reactor outfitted with two 200 W xenon bulbs positioned on opposite sides of the reactor.[36] In each experiment, a 250 mL conical flask was used to combine a photocatalyst weighing 0.010 g with a dye solution having a concentration of 10 ppm. In an effort to achieve adsorption–desorption equilibrium, the mixture was stirred continuously for thirty minutes while in the dark. Following the initial phase, a 10 mL volume of the suspension was promptly withdrawn and centrifuged to separate the photocatalyst from the dye solution. A UV-Vis

spectrophotometer (Shimadzu UV-2600 I) was used to analyze the UV-visible absorption spectra of the collected supernatant. The spectra covered a wide range of wavelengths, from 200 to 800 nanometers. The degree of dye degradation was assessed by monitoring the alteration in the intensity of the elementary absorption peak. The efficiency of photocatalytic degradation was computed using eqn (1):

$$E = \frac{1 - \dfrac{C}{C_0}}{100}\%$$ (1)

where C represents the concentration of the solution at a particular time (t), and C_0 represents the equilibrium concentration of the solution at the time (t_0) due to adsorption and desorption. The apparent rate constant for dye degradation was computed utilizing the Langmuir–Hinshelwood's pseudo-first-order kinetic model equation.

$$\ln\left(\frac{C_0}{C_t}\right) = k_{app}t = kKt$$ (2)

In this equation, t represents time in minutes, C represents the dye concentration in milligrams per liter, k_{app} represents the apparent rate constant in units per minute, K represents the adsorption coefficient of the dye of the present photocatalyst particle, and k represents the rate constant of the reaction in units min^{-1}.

5. Results and discussion

Within this groundbreaking framework, we present a pioneering method for synthesizing MgO-doped GCN (MgCN) nanocomposites in a single step, utilizing tulsi seed extract as a natural reducing agent for MgO nanoparticles. The facilitation of Mg^{2+} ion reduction is attributed to the bioactive constituents present in the tulsi seed extract, including flavonoids, phenolic compounds, and terpenoids. It's worth mentioning that they contain ursolic acid, triterpenoid, which is renowned for its powerful antioxidant and anti-inflammatory properties. This inherent compound amplifies the potential of the seeds for therapeutic interventions and green synthesis applications. Additionally, in order to attain the intended results, we have strictly regulated parameters, including reaction time and concentrations, while meticulously optimizing the synthesis conditions. These modifications have played a crucial role in improving the effectiveness and efficiency of the synthesis procedure, which has ultimately resulted in the successful fabrication of MgO-doped g-C$_3$N$_4$ nanocomposites of superior quality, which exhibit potential for diverse applications.

5.1 Phytochemical screening of tulsi seed extract

The outcomes of the qualitative phytochemical screening (QPS) of the tulsi seed extract are encapsulated in Table 1, which elucidates the presence of saponins, phenolics and tannins, flavonoids, carbohydrates, and/or glycosides, while indicating the absence of steroids, triterpenoids, and alkaloids.[37] The identified phytochemicals may play a pivotal role in the bioreduction of metal salts into nanoscale particles.[38]

28068 | *Phys. Chem. Chem. Phys.*, 2024, **26**, 28064–28081

This journal is © the Owner Societies 2024

Inference	Phytoconstituents	Name of detection test
+	Proteins/vitamins	Biuret
+	Carbohydrates	Molisch's
−	Alkaloids	Wagner's
+	Flavonoids	Lead acetate
+	Phenolics and tannins	Ferric chloride
−	Triterpenoids	Salkowski
−	Steroids	Liebermann
+	Saponins	Frothing

(+): present; (−): absent.

5.2 XRD analysis

Fig. 4 illustrates the X-ray diffraction (XRD) patterns of the MgCN hybrid nanocomposite, MgO, and purified g-C$_3$N$_4$. The diffraction planes designated as (200) are linked to the prominent peaks in the g-C$_3$N$_4$ XRD spectra at 27.61° (Fig. 4(a)).[39] Specifically, these peaks indicate the existence of specific molecular units and aromatic groups within the layers of g-C$_3$N$_4$.[40] The interlayer spacing (d = 3.24 Å) of g-C$_3$N$_4$ is represented by the peak at 2θ = 27.61°. The XRD analysis of the MgO nanoparticles exhibits distinct, pointed peaks at 2θ = 31.79°, 42.83°, and 62.14°, in accordance with the (220), (200), and (111) planes of MgO (Fig. 4(b)). The successful integration of g-C$_3$N$_4$ and MgO has resulted in a synergistic nanocomposite with the potential for improved photocatalytic activity,[41] as demonstrated by the presence of peaks corresponding to both components in the hybrid XRD spectrum of MgCN. In addition, the present structure was also ascribed to the diffraction peaks observed at 2θ = 27.3° (Fig. 4(c)).

To estimate the crystallite sizes (D) of MgO nanoparticles and MgO doped g-C$_3$N$_4$ (MgCN) nanocomposites, the Debye–Scherrer formula FWHM (full-width at half maxima) of the intense diffraction peak corresponding to the (200) peak plane of the MgCN nanocomposites[42] was used, as shown in Table 1.

$$D = 0.9\lambda/\beta \cos\theta$$

5.3 FTIR analysis

The FTIR spectra of MgO, g-C$_3$N$_4$, and MgCN nanocomposites are illustrated in Fig. 5. A broadband at 3324 cm^{-1} is indicative of a N–H bond at –NH$_2$ and –NH, while a bond observed at 808 cm^{-1} in the g-C$_3$N$_4$ spectrum corresponds to tri-s-triazine.[39]

Bands between 1343 and 1539 cm^{-1} correspond to the characteristic stretching modes of CN heterocyclic compounds. The O–H stretching mode of hydroxyl groups is represented by the peak at 3122 cm^{-1} in the MgO spectrum, which is a consequence of moisture absorption on its surface. The bending vibration of water molecules is demonstrated by the peak band at 1489 cm^{-1}, while the peaks at 878 and 678 cm^{-1} confirm the presence of MgO vibrations.[5] Additionally, the FTIR spectrum of MgO/g-C$_3$N$_4$ reveals the peaks of MgO and g-C$_3$N$_4$. Compared to the g-C$_3$N$_4$ band, the peaks in the 1320–1565 cm^{-1} range are comparatively less intense, as demonstrated in Fig. 5(a). This can be attributed to the coordination between the N atom in g-C$_3$N$_4$ and the MgO elements.[8] On the other hand, it was noticed that the intensity of the peak at 853 cm^{-1} grew stronger in the MgCN mixture (Fig. 5(b)). This could be explained by the presence of a C–O coordination bond between MgO and g-C$_3$N$_4$. Mg atoms coordinate with N atoms in g-C$_3$N$_4$, resulting in the N–C–N vibration, which is represented by the peak at 2163 cm^{-1}. The peak observed at 3236 cm^{-1} is attributed to N–H bonding.

5.4 FESEM

The synthesized g-C$_3$N$_4$, depicted in Fig. 6(a) and (b) *via* FESEM, is cohesive and resembles a cauliflower in appearance.[43] The homogeneous synthesis of MgO nanoparticles is validated by the FESEM images of the developed MgO displayed in Fig. 6(c) and (d). The FESEM images of the composite MgO NPs/g-C$_3$N$_4$ (MgCN) are displayed in Fig. 6(e)–(g).

5.5 HRTEM analysis

The HRTEM examination of g-C$_3$N$_4$ doped with MgO regularly uncovers a two-dimensional irregular morphology resembling sheets or particles measuring 30 nm in thickness (Fig. 7(a)). Consistent with the crystallite size approximated by XRD analysis, the MgO nanoparticles in the MgCN nanocomposite are typically between 35 and 50 nanometers in diameter depicted from Fig. 7(d). The MgO nanoparticles are widely dispersed and uniformly distributed across the sheet-like g-C$_3$N$_4$, creating self-active sites on the surface of the composite material, as evidenced by the HRTEM images (Fig. 7(b)). Insights regarding the microstructure of the g-C$_3$N$_4$ nanocomposite doped with MgO can also be obtained through HRTEM analysis. This includes measurements of the pore volume, volume, and surface area. The annealing temperature's impact on the lattice parameter and crystallinity,[44] in addition to the presence of oxygen vacancies and their influence on the material's crystallinity, can be discerned *via* transmission electron microscopy

Table 1 Crystallite size, interplaner spacing, dislocation density and lattice parameters of g-C$_3$N$_4$, MgO nanoparticles, and MgCN nanocomposites

Name of compound	Crystallite size (nm)	Interplanar spacing d (Å)	Dislocation density δ (nm^{-2}) $\times$ 10^{-3}	Lattice parameter (Å)
g-C$_3$N$_4$	6.62	0.512	0.006828	1.024
MgO NPs	20.6	0.516	0.00843	1.032
MgCN (0.5 mM)	25.71	0.4522	0.009103	0.9044
MgCN (1.0 mM)	34.10	0.3911	0.008954	0.7822
MgCN (1.5 mM)	41.73	0.3696	0.008575	0.7392
MgCN (2.0 mM)	39.92	0.3894	0.008273	0.7788

This journal is © the Owner Societies 2024

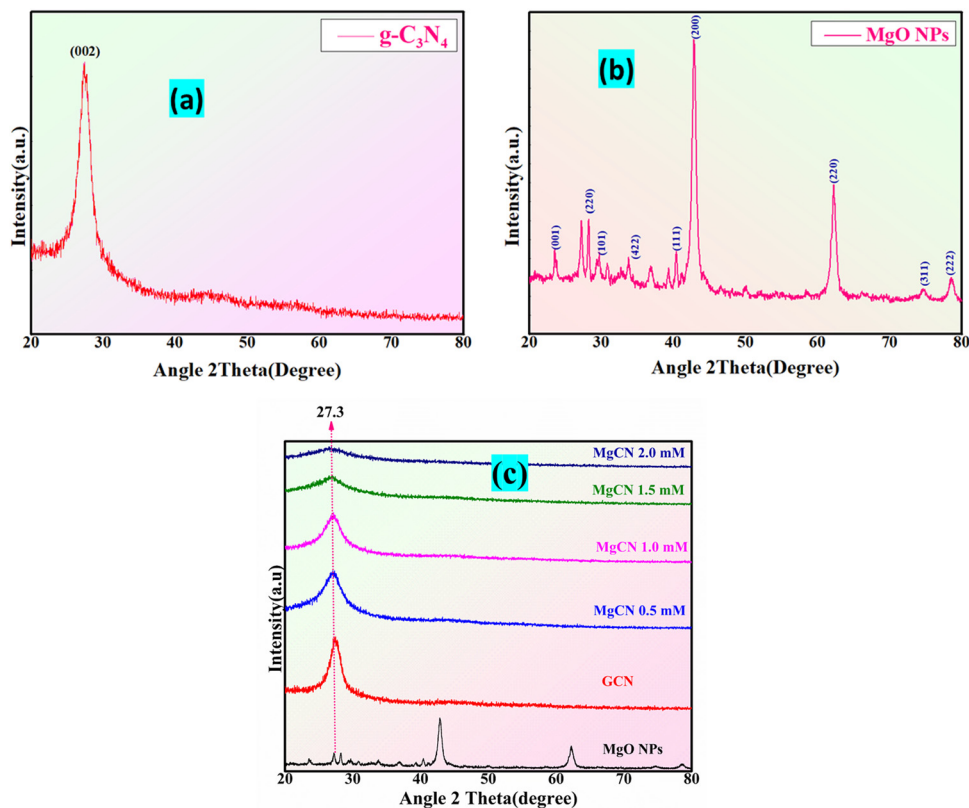*Phys. Chem. Chem. Phys.*, 2024, **26**, 28064–28081 | **28069**

Fig. 4 XRD pattern of (a) g-C_3N_4, (b) MgO NPs, and (c) MgCN composites at varied conc. (0.5, 1.0, 1.5 and 2.0 mM).
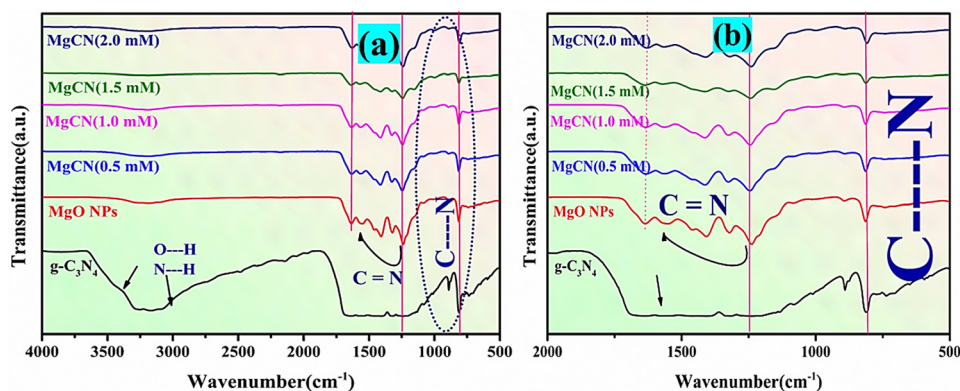

Fig. 5 FTIR spectra of (a) g-C_3N_4, MgO NPs, and MgCN nanocomposites, and (b) inset view of the MgCN bonding structure.

analysis (Park *et al.*, 2024). Fig. 7(c) also displays the SAED pattern of the MgCN nanocomposite, which illustrates the appropriate electron distribution. The analysis can provide crucial information regarding the successful incorporation of MgO into the g-C_3N_4 matrix, as well as the formation of self-active sites on the composite material's surface, which is critical for understanding the composite material's properties and prospective applications.[45–49]

5.6 TGA analysis

In order to ascertain the MgO content of the final products, thermogravimetric analysis was performed under ideal conditions at a rate of 10 °C min^{-1} from 30 to 800 °C (Toghan *et al.*, 2021). Based on the data depicted in Fig. 8, it is apparent that purified MgO experiences approx. 20% weight loss within the temperature range of 30 to 800 °C. Accelerated weight loss was observed in g-C_3N_4 nanoparticles within the temperature range of 520 to 680 °C, which is indicative of g-C_3N_4 combustion. Concurrently, the combustion of graphitic carbon nitride is indicated by a rapid decrease in the weight of MgO-doped g-C_3N_4 composites at temperatures around 535 °C. This result can be attributed to the absorption and maintenance of aerially reactive O_2 by MgO, which oxidizes graphitic carbon nitride. The quantification of MgO present in the nanocomposites was readily accomplished through sample weighing while subjected
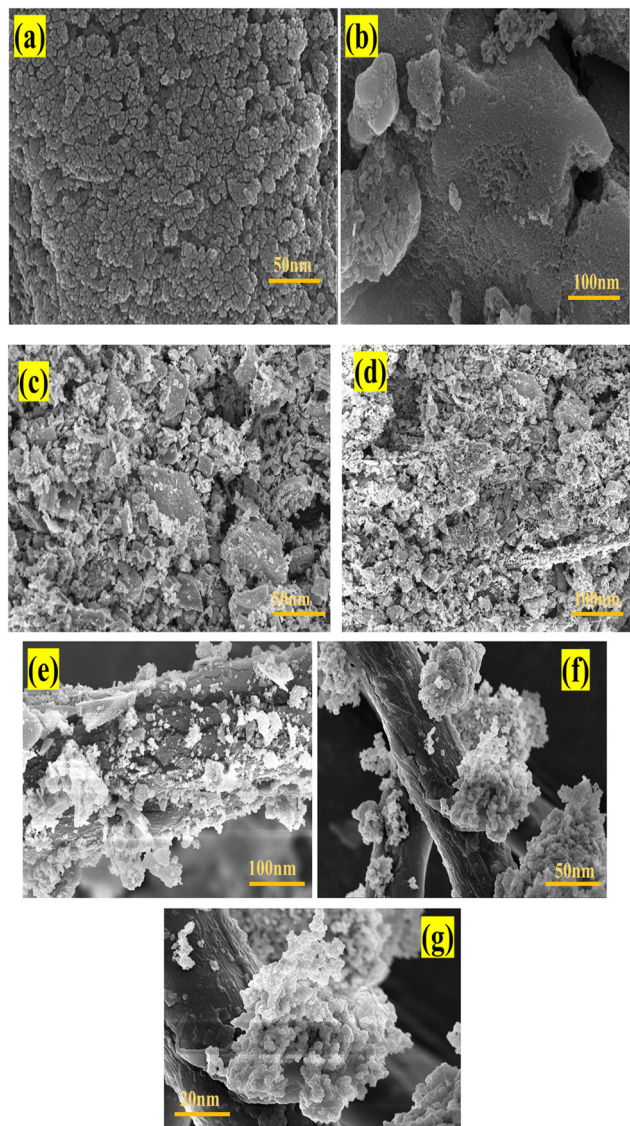
28070 | *Phys. Chem. Chem. Phys.*, 2024, **26**, 28064–28081

This journal is © the Owner Societies 2024

Fig. 6 FESEM images of g-C_3N_4 (a), (b), MgO NPs (c), (d) and MgCN nanocomposites (e)–(g) at different magnifications.

to heat at an approximate temperature of 800 °C (Wang *et al.*, 2014). The residual weight loss of all synthesized nanoparticles and nanocomposites has been shown below in Table 2.

5.7 BET analysis:

Fig. 9(a) and (b) display the N_2 adsorption and desorption isotherms of the MgCN (1.5 mM) nanocomposite. The samples exhibit type IV isotherms with a deep hysteresis loop in the improved P/P_0 range, showing their mesoporous nature. In the case of g-C_3N_4, MgO, and MgCN, the BET surface areas are 152, 37, and 84 m^2 g^{-1}, respectively, as shown in Table 3. As a consequence of MgO partially occupying the interstitial spaces in g-C_3N_4, the specific surface area of the composite has decreased, as indicated by the fall in surface area observed for the MgCN composite (Mao *et al.*, 2019b). This decrease in surface area fits the inclusion of some of the exposed gaps by MgO

nanoparticles. Uniform and narrow-down pores with diameters of 28 and 40 Å are depicted in the pore size distribution graphs (Fig. 9(c) and (d) inset). The total pore count for BJH adsorption rose from 0.39 to 0.59 cm^3 g^{-1} following the hybridization of MgO with g-C_3N_4 (0.95 cm^3 g^{-1}). The pore-size distribution plot of the MgCN opposite is also depicted in Fig. 9(e). The formation of the MgCN composite enhances the specific surface area of MgO, thereby improving its adsorption capacity for organic dyes and increasing the number of reactive sites available for the photo-catalytic process (Madona *et al.*, 2022). This, in turn, amplifies the photocatalytic performance of the material.

5.8 XPS analysis:

The X-ray photoelectron spectroscopy (XPS) analysis was conducted to evaluate the chemical composition of the MgCN nanocomposite (refer to Fig. 10). The XPS spectrum revealed distinct peaks corresponding to the elemental constituents of carbon (C), nitrogen (N), oxygen (O), and magnesium (Mg), highlighting the effective integration of MgO onto the g-C_3N_4 surface (Fig. S1, ESI†). The observed C 1s peak at 289 eV indicates the existence of covalent bonding between carbon and nitrogen species, as suggested by previous studies.[50] The distinctive Mg 2s and Mg 2p peaks of MgO are represented by peaks at 451 eV and 489 eV in the XPS spectrum of the MgCN composite, respectively. Furthermore, the Mg–O bonding formation is confirmed by the peaks at O 1s. The XPS data conclusively indicate that the primitive elements present in the composite are O, N, Mg, and C, thereby confirming the absence of any impurities and supporting prior findings related to the MgO-doped g-C_3N_4 composite.[51] This consistency with existing literature provides further validation of the results.

5.9 Optical properties of MgCN nanocomposites

The UV-Vis DRS band gap of the MgO, MgCN composite photocatalyst, g-C_3N_4, and MgO is shown in Fig. 11. With an optical edge at 380 nm, the MgO sample displayed a relatively low photon absorption while both the graphitic carbon nitride and MgCN showed an optical absorption at roughly 470 and 490–520 nm, respectively. Direct and indirect transitions help optical transitions in semiconductor materials to be computed with the Kubelka–Munk formula (Kermani *et al.*, 2020).

$$\alpha h\nu = \beta(h\nu - E_g)^n$$

where the variables ν, E_g, β, and h indicate the energy band gap of semiconductors (eV), light frequency (s^{-1}), Planck's constant (J s^{-1}), and absorption constant, respectively. The absorption coefficient (α) can be expressed as ($[2.303 \times Abs]/d$) using Beer–Lambert's law, where d and Abs are the sample thickness and absorbance, accordingly.[52] The index n for electronic transitions allowed as direct, indirect, or forbidden is assigned different values of 1/2, 2, 3/2, and 3. Another way to estimate the band gap is by using the following equation:

$$\alpha h\nu = A(h\nu - E_g)^{n/2}$$

The constant A and the semiconductor's optical transition characteristics govern the factor n. For a direct transition, n is 1,
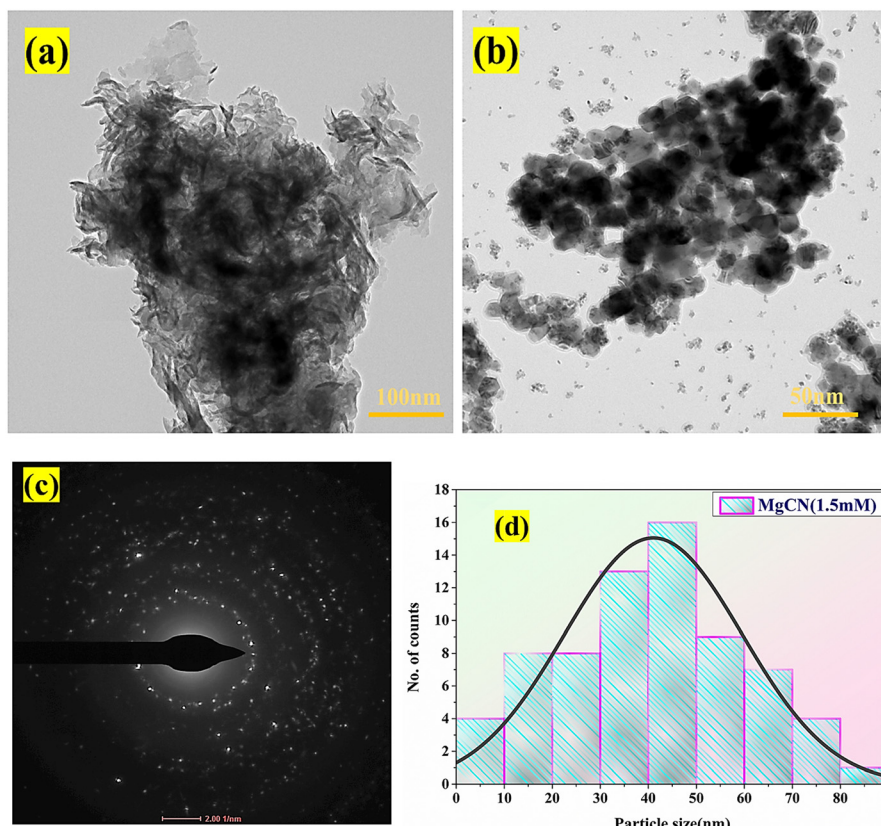
This journal is © the Owner Societies 2024

Phys. Chem. Chem. Phys., 2024, **26**, 28064–28081 | **28071**

Fig. 7 HRTEM images of (a), (b) the MgCN nanocomposite (1.5 mM) at different resolution, and SAED pattern of the prepared nanocomposites (c) along with the particle size distribution (d) of the synthesized MgCN nanocomposites.
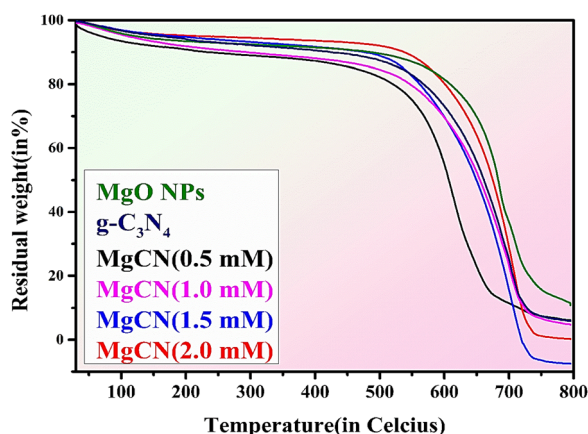

Fig. 8 Thermogravimetric analysis (TGA) spectra of the synthesized MgO NPs, g-C_3N_4 and MgCN nanocomposites.

Table 2 Percentage of weight loss in TGA

S. no.	Name of samples	% weight loss
1.	g-C_3N_4	15
2.	MgO NPs	20
2.	MgCN 0.5 mM	14.70
3.	MgCN 1.0 mM	11.8
4.	MgCN 1.5 mM	0.050
5.	MgCN 2.0 mM	9.40

5.10. Photocatalytic and kinetic activity of the MgCN nanocomposites

The performance of MgO, g-C_3N_4, and the MgCN (Fig. 13(a)–(f)) nanocomposite was evaluated by studying the degradation of methylene blue dye under visible light for a period of 120 minutes. Based on the experimental results, it is evident that the MgCN composite showcases significantly enhanced photocatalytic activity. It achieves an impressive dye degradation efficiency of 98%, surpassing the performance of g-C_3N_4 and MgO, which achieve 80% and 74% efficiency, respectively (Fig. 12). The MgO/g-C_3N_4 composite's improved photocatalytic efficiency is predominantly due to its strong ability to absorb visible light. The apparent rate constant is also shown in Table 4.

To evaluate the catalytic efficacy of the resulting nanocomposites, tetracycline (TC) was used as a model antibiotic.[53] Both
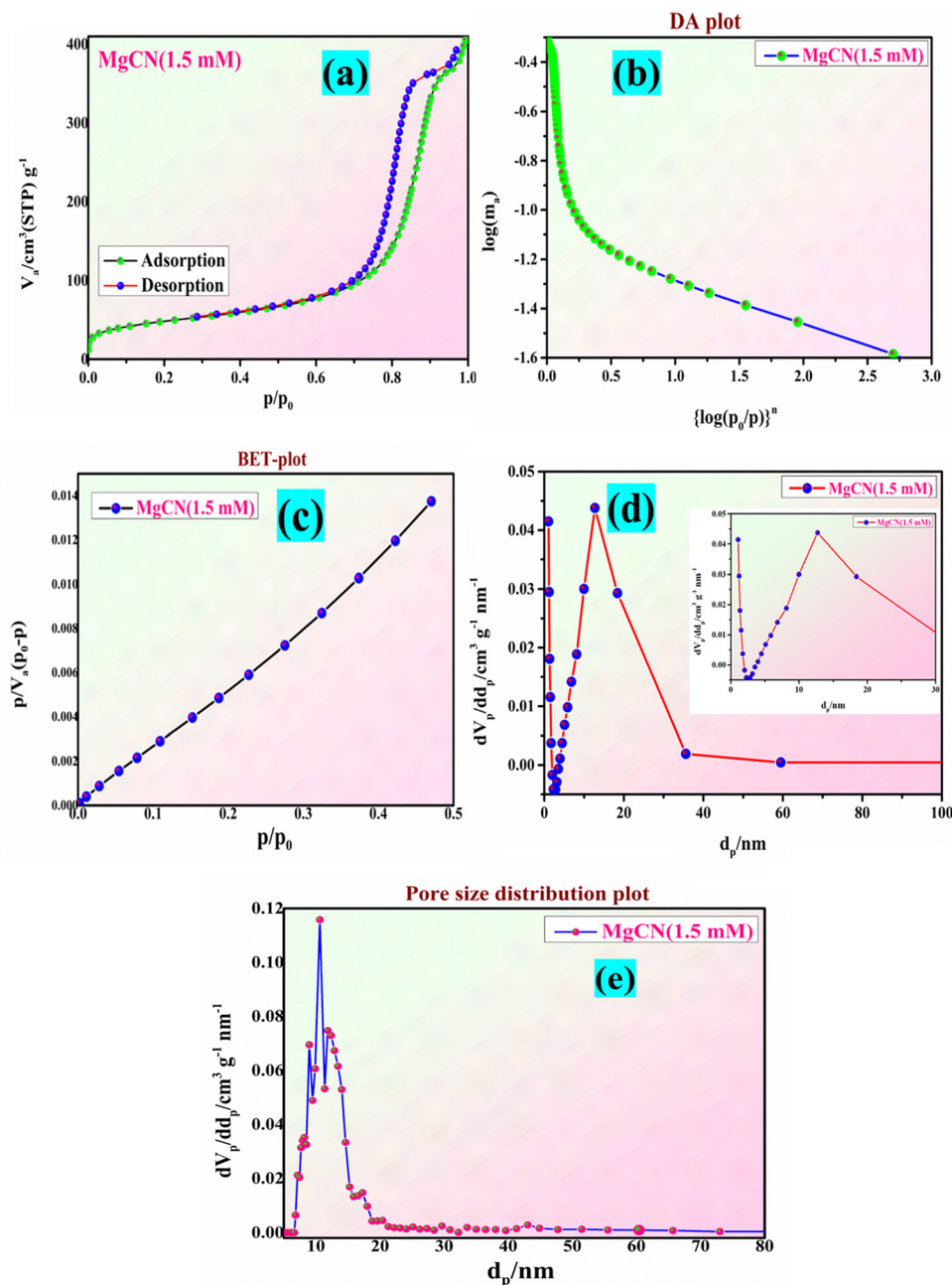
while for an indirect transition, it is 4. The estimated band gaps of MgO, g-C_3N_4, and MgCN (0.5, 1.0, 1.5 and 2.0 mM) were 5.51, 2.71, 5.32, 5.13, 5.03 and 4.89 eV, respectively. The band gaps have decreased following the coupling of MgO and g-C_3N_4, suggesting that the composite photocatalysts are capable of efficiently absorbing in the visible light region, resulting in the generation of additional electron–hole pairs that strengthen their photocatalytic activity.

28072 | *Phys. Chem. Chem. Phys.*, 2024, **26**, 28064–28081

This journal is © the Owner Societies 2024

Fig. 9 The adsorption–desorption adsorption-surface area curve of the (a) and (b) MgO/g-C$_3$N$_4$ nanocomposite (MgCN), together with the BET and BJH plot (c) and (d) (inset view) and the pore distribution curve (e).

Table 3 BET particle size, surface area, pore volume, and pore diameter of the MgCN nanocomposite

Sample	Particle size (nm)	Surface area (m^2 g^{-1})	Pore volume (cm^3 g^{-1})	Pore diameter (nm)
MgO	39.06	37	0.39	9.58
g-C$_3$N$_4$	46.89	152	0.59	4.55
MgCN (1.5 mM)	44.23	84	0.95	12.08

g-C$_3$N$_4$ and MgO did not catalyze the breakdown of tetracycline, suggesting no catalytic activity under experimental circumstances. The MgCN nanocomposite contains foremost singlet oxygen (^{1}O$_2$) and minor hydroxyl radicals ($^\bullet$OH) that respond to TC degradation. The degradation extends up to 54% by using composite MgCN (1.5 mM).

5.11. Effect of pH and catalyst dosage

The pH of the solution is a vital variable in photocatalysis as it affects both the surface functionality of the catalyst and the ionization state of the dye molecule. The variation in the percentage of photocatalysis between pH (3–11) is depicted in Fig. 14(a). The photocatalyst exhibits a significantly diminished efficacy at low pH.[54] This is due to the fact that MgO within the
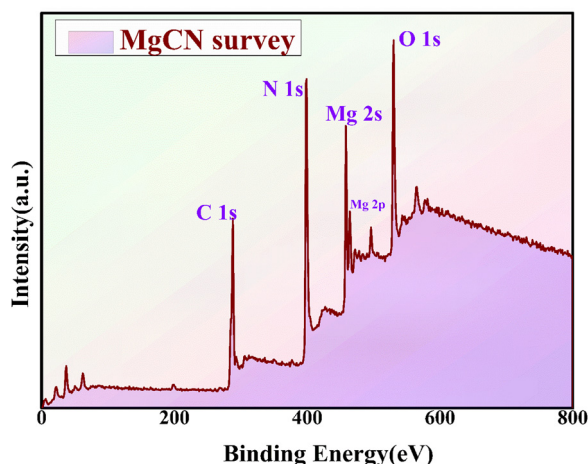
This journal is © the Owner Societies 2024

Phys. Chem. Chem. Phys., 2024, **26**, 28064–28081 | **28073**

Fig. 10   XPS survey spectra for the MgCN nanocomposite.

MgCN nanocomposite reacts with the available H$^+$ in the solution at low pH and dissolves completely in the solution.[55] Furthermore, at such a low pH, the positively charged H$^+$ ions form complexes with the negatively charged dyes, therefore reducing the electrostatic bonds with the nanocomposite's active sites. Conversely, in acidic environments with a pH between 7, 9, and 11, the surface charge is negative, which forces the dye molecules to resist adsorption *via* coulombic repulsion; this results in a noticeable decrease in efficacy.[56] Based on the composite's pH value of 5–7, its surface exhibits a positive charge at pH values greater than pH$_{pzc}$ and a negative charge at pH values less than pH$_{pzc}$.[57] The optimal condition for dye removal is achieved at alkaline solution conditions, as evidenced by the best efficiency seen at pH = 9.

The amount that exists of the photocatalyst affects the degradation of the dye. An increase in the cumulative dose of the catalyst distinguishes heterogeneous photocatalysis by means of dye degradation. This is a clear result of the photo-catalyst surface's increased active sites, which in turn causes the production of radicals that contribute to the staining of the dye solution.[58] The murky nature of the solution starts to limit incident radiation as the catalyst level exceeds a particular threshold, hence lowering the dye degradation.[59] In order to investigate how the dose of the MgCN nanocomposite affected the degradation of both (methylene and crystal violet) dyes, five different doses—3, 6, 9, 12 and 15 mg l^{-1} were selected (Fig. 14(b)), and the photodegradation was measured during a 100-minute period. The dye degradation percentage reached 20, 45, 62, 64 and 89 for doses of 3, 6, 9, 12 and 15 mg l^{-1}, respectively. This indicates that a complete dye degradation was achieved with a dose of 9 mg l^{-1} of MgCN.

5.12. Scavenging experiments

The MgCN nanocomposite system was employed to identify the primary reactive species involved in the photocatalytic degradation of methylene dye. The results of active species trapping experiments are depicted in the figure (Fig. 15). A second-order reaction between methanol and O$_2^-$ occurs throughout the photocatalytic process, indicating that O$_2^-$ is the main species involved.[60] This is demonstrated by the significant photodegradation rates discovered in methanol. Indicating the involvement of electrons in the decolorization of the dye, the AgNO$_3$ substantially inhibited degradation. Further evidence that the holes have less of an impact comes from DMSO, which shows a slight decline in photodegradation (Park *et al.*, 2024b). Furthermore, the addition of nitrates and sulfates did not appreciably
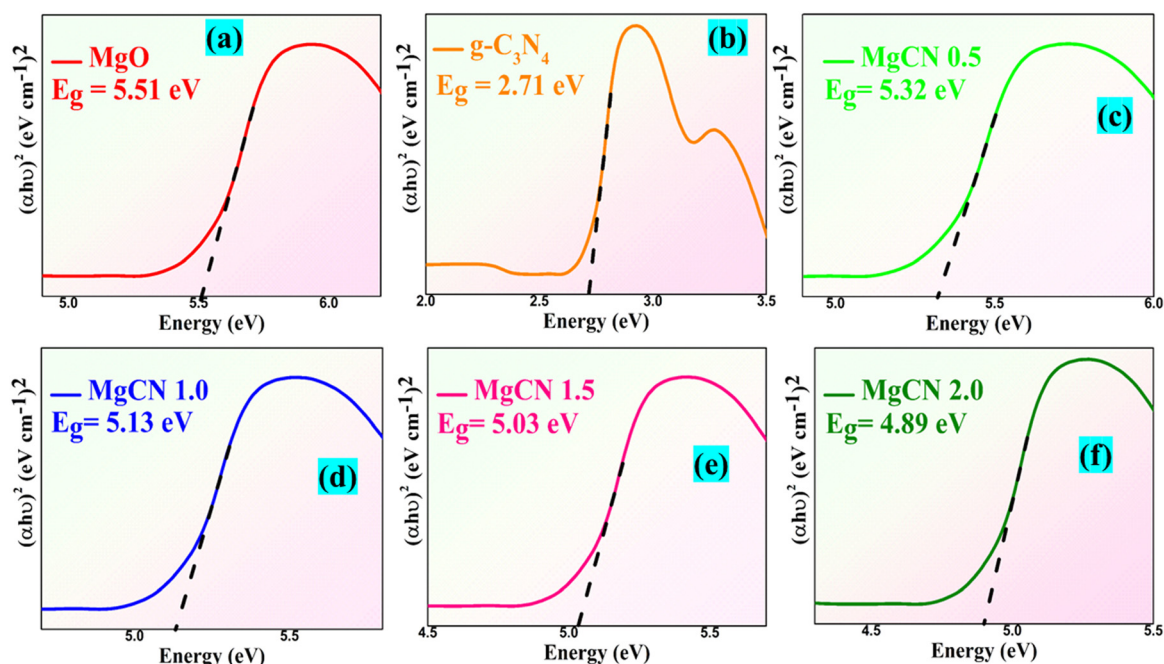

Fig. 11   UV-Vis assisted bandgaps of the MgO (a), g-C$_3$N$_4$ (b), and MgCN nanocomposite at 0.5, 1.0, 1.5, and 2.0 mM (c)–(f), respectively.

28074 | *Phys. Chem. Chem. Phys.*, 2024, **26**, 28064–28081

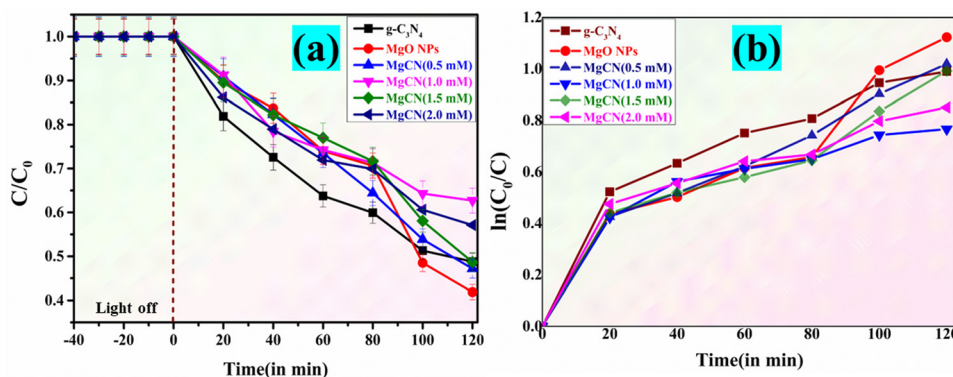This journal is © the Owner Societies 2024

Fig. 12 (a) C/C_0 Comparison of the degradation of Methylene Blue dye (dark and light mode); (b) ln C_0/C_t as a function of visible light irradiation period with MgO, g-C_3N_4 and MgCN nanocomposites.

Table 4 Apparent rate constant and degradation efficiency of the dye

S. no.	Samples	Degradation efficiency MB dye (%)	Apparent rate constant (k) min^{-1}
1.	g-C_3N_4	80	0.007941
2.	MgO NPs	74	0.008085
3.	MgCN 0.5 mM	88	0.008676
4.	MgCN 1.0 mM	92	0.008792
5.	MgCN 1.5 mM	98	0.009671
6.	MgCN 2.0 mM	96	0.008904

delay the photodegradation of methylene dye, suggesting that the $^\bullet$OH radical was not thoroughly involved in the process.[61,62]

5.13. Mechanism of photodegradation

The CB and VB values of MgCN are determined. The equations for calculating E_{CB} and E_{VB} are as follows (Sha *et al.*, 2024):

$$E_{CB} = X - E_C - 0.5E_g$$

$$E_{VB} = E_{CB} + E_g$$

The spatial separation of photogenerated charge carriers within the Z-scheme photocatalytic framework is mostly responsible for the improved photocatalytic activity in binary composites, including g-C_3N_4 and MgO. Under this system, g-C_3N_4 absorbs visible light photons, which causes electron excitation from the valence band (VB) to the conduction band (CB), hence producing holes (h$^+$) in the valence band (VB). By interfacial contact, these excited electrons then migrate from the CB of g-C_3N_4 to the CB of MgO, hence obtaining effective spatial separation of electrons and holes.[63] This separation enables the formation of reactive superoxide radicals ($^\bullet$O$_2^-$) when these electrons interact with adsorbed O$_2$ on the composite's surface.[64] This is evident in the VB potential of 1.656 eV *vs.* NHE for g-C_3N_4, which is less positive than the oxidation potential of OH$^-$/$^\bullet$OH (2.35 V *vs.* NHE). Subsequently, the g-C_3N_4 VB holes cannot produce $^\bullet$OH radicals, which corroborates the results of radical scavenger experiments.[65] The direct oxidation of dyes, such as methylene blue, is facilitated by photogenerated pores and reactive $^\bullet$O$_2^-$ in the photodegradation process. Anionic sulfonic

acid groups promote adsorption on the composite surface, thereby accelerating the oxidation process.[66] The formation of $^\bullet$O$_2^-$ is facilitated by the substantial differential in migration rates between photogenerated electrons and holes, which reacts with the dye more rapidly than direct oxidation by holes. This mechanism corresponds with scavenger experiments showing that dye photodegradation in the MgO-doped g-C_3N_4 composite is caused by $^\bullet$O$_2^-$, electrons (e$-$), and holes (h$^+$).[67] The conclusion that g-C_3N_4 VB holes are unable to react with OH$-$/H$_2$O to form $^\bullet$OH radicals is further supported by the lower VB edge potential of g-C_3N_4 (1.83 eV) in comparison to the OH$^-$/$^\bullet$OH couple potential (2.7 eV *vs.* NHE).[68] The mechanism supports the suggested Z-scheme pathway for methylene blue dye photodegradation and is consistent with previous research as it produces more powerful oxidizing agents and increases superoxide radical production in comparison to the type II heterojunction mechanism. This is visually represented in Fig. 16, illustrating the described photodegradation mechanism.[69]

5.14. Antibacterial analysis

The agar well diffusion method was employed to investigate the antibacterial efficacy of the MgCN nanocomposite. As illustrated in Fig. 17, antibacterial activity assays were conducted against *E. coli* bacteria at variable concentrations of the nanocomposite (Paul *et al.*, 2021). The analysis of Table 5 indicates that the inhibition zone experiences a gradual expansion in conjunction with the concentration of the MgO/g-C_3N_4 nanocomposite.[70] This pattern is ascribed to the generation of reactive oxygen species (ROS), which is made possible by the MgCN (1.5 mM) nanocomposite's vast surface area and small particle size.[71] As a result, the nanocomposite effectively undermines the integrity of bacterial cells and impedes bacterial proliferation. The MgO/g-C_3N_4 nanocomposite interacts with oxygen in solution, producing excessive ROS such as oxygen peroxides, hydroxy radicals, and superoxide radicals (Raouf *et al.*, 2017). Therefore, the produced ROS may harm bacteria's DNA and cell wall membrane, inhibiting their ability to proliferate.[72]

4. Conclusion

A binary MgO-doped g-C_3N_4 composite was synthesized in this investigation through a facile green synthesis approach

This journal is © the Owner Societies 2024

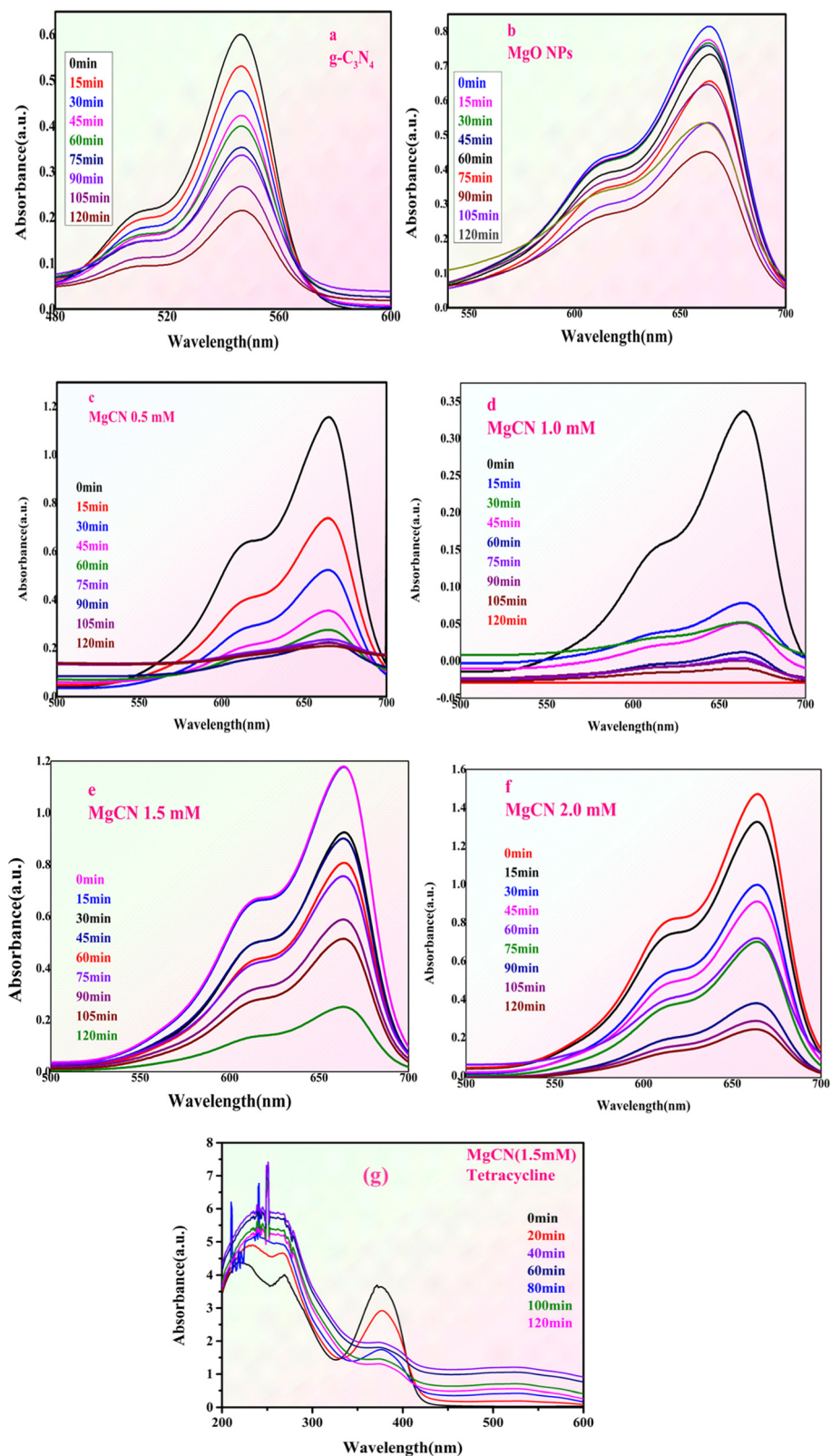*Phys. Chem. Chem. Phys.*, 2024, **26**, 28064–28081 | **28075**

Fig. 13 shows the methylene blue dye degradation spectra of (a) g-C_3N_4, (b) MgO NPs, and (c)–(f) MgO doped g-C_3N_4 NCs at different concentrations, together with the tetracycline antibiotic degradation spectra (g).
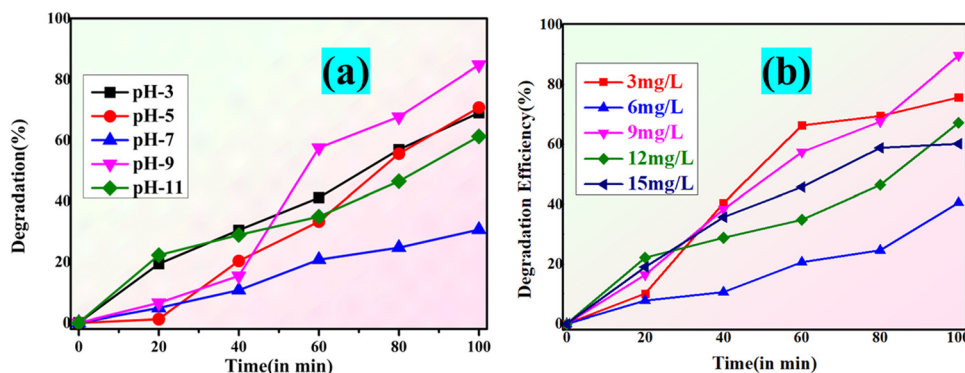
28076 | *Phys. Chem. Chem. Phys.*, 2024, **26**, 28064–28081

This journal is © the Owner Societies 2024

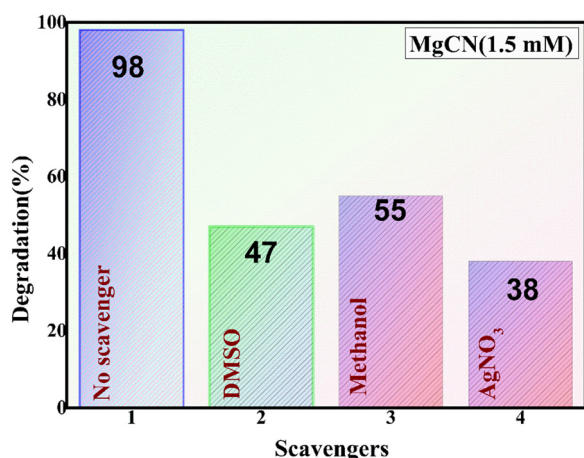**Fig. 14** Degradation percentage and photocatalytic degradation of methylene blue dye at varying pH (a) and MgCN nanocomposite catalyst dosage (b).

Fig. 15 Effect of radical scavenging compounds on the photodegradation of methylene dye.

utilizing tulsi seeds as the reducing as well as capping agent. Subsequently, the composite was extensively characterized using various techniques. The presence of distinct peaks corresponding to g-C$_3$N$_4$ and MgO was confirmed through XRD and FTIR analyses, indicating their formation. The purity of the synthesized materials was further confirmed through X-ray photoelectron spectroscopy. The surface area analysis using the BET method showed an increase in surface area, which resulted in enhanced photodegradation performance. The efficiency of the MgCN composite in breaking down methylene blue dye was studied and compared to its precursors, MgO and g-C$_3$N$_4$. The results showed that the composite material had a higher capacity for degradation. The photocatalytic degradation process depends critically on $^\bullet O_2^-$, e^-, and h^+, as demonstrated by the radical scavenger tests. The most potent antibacterial activity was found at a concentration of 75 μg l^{-1}, owing to the production of ROS (OH$^\bullet$, O$_2{}^{\bullet-}$). As an outcome, the synthesized MgCN nanocomposite is a perfect catalyst for eliminating organic contaminants and exhibiting antibacterial properties. The significance of utilizing synergistic approaches to tackle contemporary environmental challenges is highlighted as this research paves the way for the development of environmentally benign, efficient, and cost-effective photocatalytic systems for remediation purposes.
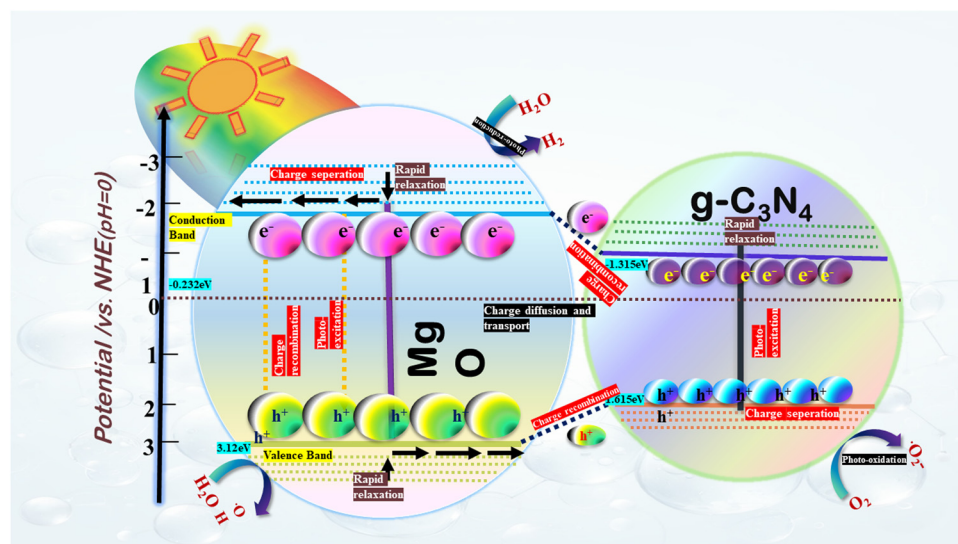

Fig. 16 Devised Z-scheme mechanism for the synthesized MgCN nanocomposite for degradation of methylene blue dye.

This journal is © the Owner Societies 2024

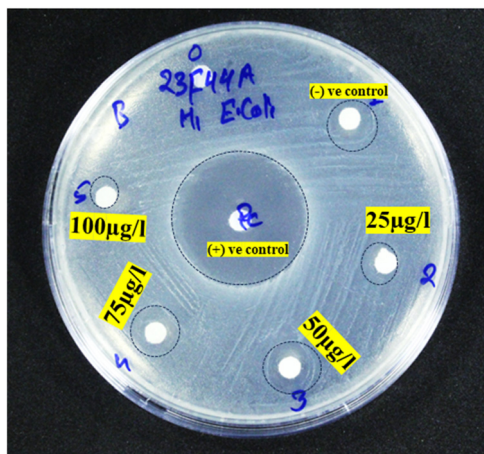*Phys. Chem. Chem. Phys.*, 2024, **26**, 28064–28081 | **28077**

Fig. 17 Antibacterial activity of the MgCN (1.5 mM) nanocomposite.

Table 5 Antibacterial activity of the MgCN (1.5 mM) nanocomposite showing their zone of inhibition at varied conc

| | | | | Antibacterial activity of MgCN (1.5 mM) nanocomposite | | | |
| | | | | Zone of inhibition in (mm) | | | |
Type of bacteria	Performed bacteria	Standard (tetracycline)	Negative control	25 µl	50 µl	75 µl	100 µl
Gram negative	*E. coli*	10	—	2	4	6	2.5

Ethical approval

The research submitted is carried out in compliance with relevant institutional biosafety and biosecurity protocols.

Consent to participate

Informed consent was obtained from all individual participants included in the study.

Consent to publish

The authors affirm that participants provided informed consent for the publication of all images in the figures.

Author contributions

All authors contributed to study conception and design. Sweety: conceptualization; methodology; validation; roles/writing – original draft; Anshu Sharma: supervision, conceptualization, methodology, roles/writing – original draft, writing – review and editing; Sudesh Chaudhary: supervision; conceptualization; methodology; roles/writing – original draft; writing – review and editing.

Data availability

Supplementary data and material will be published as received from the author.

Conflicts of interest

The authors declare no conflict of interest.

References

1 S. Sharma, V. Dutta, P. Singh, P. Raizada, A. Rahmani-Sani, A. Hosseini-Bandegharaei and V. K. Thakur, *J. Cleaner Prod.*, 2019, **228**, 755–769.

2 D. Bhatia, N. R. Sharma, J. Singh and R. S. Kanwar, Biological methods for textile dye removal from wastewater: A review, *Crit. Rev. Environ. Sci. Technol.*, 2017, **47**, 1836–1876.

3 G. K. Naik, P. M. Mishra and K. Parida, Green synthesis of Au/TiO$_2$ for effective dye degradation in aqueous system, *Chem. Eng. J.*, 2013, **229**, 492–497.

4 E. M. Cuerda-correa, M. F. Alexandre-franco and C. Fern, Antibiotics from Water. An Overview, *Water*, 2020, **12**(1), 10.

5 S. Kumar Kuila, P. Kumbhakar, C. Sekhar Tiwary and T. Kumar Kundu, Photon and vibration synergism on planar defects induced 2D-graphitic carbon nitride for ultrafast remediation of dyes and antibiotic ampicillin, *J. Mater. Sci.*, 2022, **57**, 8658–8675.

6 N. N. Mahamuni and Y. G. Adewuyi, Advanced oxidation processes (AOPs) involving ultrasound for waste water treatment: A review with emphasis on cost estimation, *Ultrason. Sonochem.*, 2010, **17**, 990–1003.

7 T. Wang, X. Jin, Z. Chen, M. Megharaj and R. Naidu, Green synthesis of Fe nanoparticles using eucalyptus leaf extracts for treatment of eutrophic wastewater, *Sci. Total Environ.*, 2014, **466–467**, 210–213.

8 L. Ge, Y. Yue, W. Wang, F. Tan, S. Zhang, X. Wang, X. Qiao and P. K. Wong, Efficient degradation of tetracycline in wide pH range using MgNCN/MgO nanocomposites as novel H$_2$O$_2$ activator, *Water Res.*, 2021, **198**, 117149, DOI: **10.1016/j.watres.2021.117149**.

9 M. R. Hoffmann, S. T. Martin, W. Choi and D. W. Bahnemann, Environmental Applications of Semiconductor Photocatalysis, *Chem. Rev.*, 1995, **95**, 69–96.

28078 | *Phys. Chem. Chem. Phys.*, 2024, **26**, 28064–28081

This journal is © the Owner Societies 2024

10 X. Wang, S. Blechert and M. Antonietti, *ACS Catal.*, 2012, **2**, 1596–1606.

11 M. S. Nasir, G. Yang, I. Ayub, S. Wang, L. Wang, X. Wang, W. Yan, S. Peng and S. Ramakarishna, *Appl. Catal., B*, 2019, 257.

12 J. Zhu, P. Xiao, H. Li and A. C. Carabineiro, Graphitic Carbon Nitride: Synthesis, Properties, and Applications in Catalysis, *ACS Appl. Mater. Interfaces*, 2014, **6**(19), 16449–16465, DOI: **10.1021/am502925j**.

13 M. Zimbone, M. A. Buccheri, G. Cacciato, R. Sanz, G. Rappazzo, S. Boninelli, R. Reitano, L. Romano, V. Privitera and M. G. Grimaldi, Photocatalytical and antibacterial activity of TiO2 nanoparticles obtained by laser ablation in water, *Appl. Catal., B*, 2015, **165**, 487–494.

14 N. Zhang, L. Wen, J. Yan and Y. Liu, Dye-sensitized graphitic carbon nitride (g-C$_3$N$_4$) for photocatalysis: a brief review, *Chem. Pap.*, 2020, **74**, 389–406.

15 P. Wang, J. Wang, X. Wang, H. Yu, J. Yu, M. Lei and Y. Wang, One-step synthesis of easy-recycling TiO$_2$–rGO nanocomposite photocatalysts with enhanced photocatalytic activity, *Appl. Catal., B*, 2013, **132–133**, 452–459.

16 S. Pu, R. Zhu, H. Ma, D. Deng, X. Pei, F. Qi and W. Chu, Facile in-situ design strategy to disperse TiO$_2$ nanoparticles on graphene for the enhanced photocatalytic degradation of rhodamine 6G, *Appl. Catal., B*, 2017, **218**, 208–219.

17 D. R. Paul and S. P. Nehra, Graphitic carbon nitride: a sustainable photocatalyst for organic pollutant degradation and antibacterial applications, *Environ. Sci. Pollut. Res. Int.*, 2021, **4**, 3888–3896.

18 L. Jiang, X. Yuan, Y. Pan, J. Liang and G. Zeng, Doping of graphitic carbon nitride for photocatalysis: A reveiw, *Appl. Catal., B*, 2017, **217**, 388–406.

19 S. Tonda, S. Kumar, S. Kandula and V. Shanker, Fe-doped and -mediated graphitic carbon nitride nanosheets for enhanced photocatalytic performance under natural sunlight, *J. Mater. Chem. A*, 2014, **2**, 6772–6780.

20 R. Vijayan, S. Joseph and B. Mathew, Anticancer, antimicrobial, antioxidant, and catalytic activities of green-synthesized silver and gold nanoparticles using Bauhinia purpurea leaf extract, *Bioprocess Biosyst. Eng.*, 2019, **42**, 305–319.

21 J. Karimi and S. Mohsenzadeh, Rapid, green, and eco-friendly biosynthesis of copper nanoparticles using flower extract of Aloe vera, *Synth. React. Inorg., Met.-Org., Nano-Met. Chem.*, 2015, **45**, 895–898.

22 G. Mamba and A. K. Mishra, Graphitic carbon nitride (g-C$_3$N$_4$) nanocomposites: A new and exciting generation of visible light driven photocatalysts for environmental pollution remediation, *Appl. Catal., B*, 2016, **198**, 347–377, DOI: **10.1016/j.apcatb.2016.05.052**.

23 P. Malik, R. Shankar, V. Malik, N. Sharma and T. K. Mukherjee, Green Chemistry Based Benign Routes for Nanoparticle Synthesis, *J. Nanopart.*, 2014, **2014**, 1–14.

24 S. Jadoun, R. Arif, N. K. Jangid and R. K. Meena, Green synthesis of nanoparticles using plant extracts: a review, *Environ. Chem. Lett.*, 2021, **19**, 355–374.

25 S. Gunalan, R. Sivaraj and V. Rajendran, Green synthesized ZnO nanoparticles against bacterial and fungal pathogens, *Prog. Nat. Sci.: Mater. Int.*, 2012, **22**, 693–700.

26 P. Panchal, P. Meena and S. P. Nehra, A rapid green synthesis of Ag/AgCl-NC photocatalyst for environmental applications, *Environ. Sci. Pollut. Res.*, 2021, **28**, 3972–3982.

27 S. Dahiya, R. Sharma, P. Gautam, P. Panchal, S. Chaudhary, A. Sharma, M. Almáši and S. P. Nehra, Eco-friendly phyto-fabrication of Ficus Benjamina L. based ZnO-doped g-C$_3$N$_4$ nanocomposites for remarkable photocatalysis and antibacterial applications, *Chemosphere*, 2023, **339**, 139707, DOI: **10.1016/j.chemosphere.2023.139707**.

28 P. Panchal, D. R. Paul, A. Sharma, P. Choudhary, P. Meena and S. P. Nehra, Biogenic mediated Ag/ZnO nanocomposites for photocatalytic and antibacterial activities towards disinfection of water, *J. Colloid Interface Sci.*, 2020, **563**, 370–380.

29 S. Shoran, S. Chaudhary and A. Sharma, Photocatalytic dye degradation and antibacterial activities of CeO$_2$/g-C$_3$N$_4$ nanomaterials for environmental applications, *Environ. Sci. Pollut. Res.*, 2023, **30**(44), 98682–98700, DOI: **10.1007/s11356-022-23815-x**.

30 S. Dahiya, A. Sharma and S. Chaudhary, Synthesis of phytoextract-mediated Ag-doped graphitic carbon nitride (Ag@GCN) for photocatalytic degradation of dyes, *Environ. Sci. Pollut. Res.*, 2023, **30**(10), 25650–25662, DOI: **10.1007/s11356-023-25359-0**.

31 C. Liu, L. Wang, H. Xu, S. Wang, S. Gao, X. Ji, Q. Xu and W. Lan, 'one pot' green synthesis and the antibacterial activity of g-C$_3$N$_4$/Ag nanocomposites, *Mater. Lett.*, 2016, **164**, 567–570.

32 P. Panchal, R. Malik, D. R. Paul, P. Meena, V. K. Tomer and S. P. Nehra, Photocatalytic Activity of Green Synthesized AgCl, *Nanosci. Nanotechnol.*, 2019, **19**, 5249–5255.

33 P. Panchal, D. R. Paul, A. Sharma, D. Hooda, R. Yadav, P. Meena and S. P. Nehra, Phytoextract mediated ZnO/MgO nanocomposites for photocatalytic and antibacterial activities, *J. Photochem. Photobiol., A*, 2019, **385**, 112049.

34 S. Bhakya, S. Muthukrishnan, M. Sukumaran and M. Muthukumar, Biogenic synthesis of silver nanoparticles and their antioxidant and antibacterial activity, *Appl. Nanosci.*, 2016, **6**, 755–766.

35 N. R. Farnsworth, *Biological and Phytochemical Screening of Plants*, 1966, vol. 55.

36 D. Rattan, R. Sharma, P. Panchal, S. P. Nehra, A. P. Gupta and A. Sharma, ScienceDirect Synthesis, characterization and application of silver doped graphitic carbon nitride as photocatalyst towards visible light photocatalytic hydrogen evolution, *Int. J. Hydrogen Energy*, 2020, **45**(44), 23937–23946, DOI: **10.1016/j.ijhydene.2019.06.061**.

37 K. Sen, M. Goyal and S. Mukopadayay, review on phytochemical and pharmacological, medicinal properties of holy basil (*Ocimum sanctum L.*), *Int. J. Health Sci.*, 2022, 7276–7286.

38 S. Iravani, H. Korbekandi, S. V. Mirmohammadi and B. Zolfaghari, *Synthesis of silver nanoparticles: chemical, physical and biological methods*, 2014, vol. 9.

This journal is © the Owner Societies 2024

Phys. Chem. Chem. Phys., 2024, **26**, 28064–28081 | **28079**

39 E. Fathi, F. Derakhshanfard, P. Gharbani and Z. Ghazi Tabatabaei, Facile Synthesis of MgO/C$_3$N$_4$ Nanocomposite for Removal of Reactive Orange 16 Under Visible Light, *J. Inorg. Organomet. Polym. Mater.*, 2020, **30**, 2234–2240.

40 S. Dahiya, S. Shoran, D. N. Sharma, V. S. Rao, S. Chaudhary, S. P. Nehra and A. Sharma, Bioengineered sustainable phyto-fabrication of anatase TiO$_2$-adorned g-C$_3$N$_4$ nanocomposites and unveiling their photocatalytic potential towards advanced environmental remediation, *Chemosphere*, 2024, **362**, 142456.

41 N. Mao and J. X. Jiang, MgO/g-C$_3$N$_4$ nanocomposites as efficient water splitting photocatalysts under visible light irradiation, *Appl. Surf. Sci.*, 2019, **476**, 144–150.

42 N. Kumaresan, M. M. A. Sinthiya, M. Praveen Kumar, S. Ravichandran, R. Ramesh Babu, K. Sethurman and K. Ramamurthi, Investigation on the g-C$_3$N$_4$ encapsulated ZnO nanorods heterojunction coupled with GO for effective photocatalytic activity under visible light irradiation, *Arabian J. Chem.*, 2020, **13**, 2826–2843.

43 Z. Chen, S. Zhang, Y. Liu, N. S. Alharbi, S. O. Rabah, S. Wang and X. Wang, *Sci. Total Environ.*, 2020, 731.

44 V. K. Mrunal, A. K. Vishnu, N. Momin and J. Manjanna, Cu$_2$O nanoparticles for adsorption and photocatalytic degradation of methylene blue dye from aqueous medium, *Environ. Nanotechnol., Monit. Manage.*, 2019, **12**, 100265, DOI: **10.1016/j.enmm.2019.100265**.

45 H. Kwang Benno Park, P. Kumar, I. Kebaili, I. Boukhris, Y. Hwan Joo, T. Hyun Sung and A. Kumar, Optimization and modelling of magnesium oxide (MgO) photocatalytic degradation of binary dyes using response surface methodology, *Sci. Rep.*, 2024, **14**(1), 9412, DOI: **10.1038/s41598-024-56797-6**.

46 A. Toghan and A. Modwi, Boosting unprecedented indigo carmine dye photodegradation *via* mesoporous MgO@g-C$_3$N$_4$ nanocomposite, *J. Photochem. Photobiol., A*, 2021, **419**, 113467, DOI: **10.1016/j.jphotochem.2021.113467**.

47 P. Wang, D. Li, J. Chen, X. Zhang, J. Xian, X. Yang, X. Zheng, X. Li and Y. Shao, A novel and green method to synthesize CdSe quantum dots-modified TiO$_2$ and its enhanced visible light photocatalytic activity, *Appl. Catal., B*, 2014, **160–161**, 217–226.

48 N. Mao and J. X. Jiang, MgO/g-C$_3$N$_4$ nanocomposites as efficient water splitting photocatalysts under visible light irradiation, *Appl. Surf. Sci.*, 2019, **476**, 144–150.

49 J. Madona and C. Sridevi, Surfactant assisted hydrothermal synthesis of MgO/g-C$_3$N$_4$ heterojunction nanocomposite for enhanced solar photocatalysis and antimicrobial activities, *Inorg. Chem. Commun.*, 2022, **138**, 109265, DOI: **10.1016/j.inoche.2022.109265**.

50 W. An, L. Tian, J. Hu, L. Liu, W. Cui and Y. Liang, Efficient degradation of organic pollutants by catalytic ozonation and photocatalysis synergy system using double-functional MgO/g-C$_3$N$_4$ catalyst, *Appl. Surf. Sci.*, 2020, **534**, 147518, DOI: **10.1016/j.apsusc.2020.147518**.

51 E. Fathi, F. Derakhshanfard, P. Gharbani and Z. Ghazi Tabatabaei, Facile Synthesis of MgO/C$_3$N$_4$ Nanocomposite for Removal of Reactive Orange 16 Under Visible Light, *J. Inorg. Organomet. Polym. Mater.*, 2020, **30**, 2234–2240.

52 Z. Ren, F. Chen, K. Wen and J. Lu, Enhanced photocatalytic activity for tetracyclines degradation with Ag modified g-C$_3$N$_4$ composite under visible light, *J. Photochem. Photobiol., A*, 2024, **5**, 100116, DOI: **10.1016/j.jphotochem.2019.112217**.

53 N. Kumaresan, M. M. A. Sinthiya, M. Praveen Kumar, S. Ravichandran, R. Ramesh Babu, K. Sethurman and K. Ramamurthi, Investigation on the g-C$_3$N$_4$ encapsulated ZnO nanorods heterojunction coupled with GO for effective photocatalytic activity under visible light irradiation, *Arabian J. Chem.*, 2020, **13**, 2826–2843.

54 W. Zeng, M. Gao, K. Liu, C. Li, N. Cao, X. Zhao, J. Feng, Y. Ren and T. Wei, Boosting charge separation and surface defects for superb photocatalytic activity of magnesium oxide/graphene nanosheets, *Appl. Surf. Sci.*, 2021, **535**, 147658, DOI: **10.1016/j.apsusc.2020.147658**.

55 Z. Chen, S. Zhang, Y. Liu, N. S. Alharbi, S. O. Rabah, S. Wang and X. Wang, *Sci. Total Environ.*, 2020, 731.

56 V. K. Mrunal, A. K. Vishnu, N. Momin and J. Manjanna, Cu$_2$O nanoparticles for adsorption and photocatalytic degradation of methylene blue dye from aqueous medium, *Environ. Nanotechnol., Monit. Manage.*, 2019, **12**, 100265, DOI: **10.1016/j.enmm.2019.100265**.

57 M. Induja, K. Sivaprakash, G. Priya and S. Karthikeyan, Facile green synthesis and antimicrobial performance of Cu$_2$O nanospheres decorated g-C$_3$N$_4$ nanocomposite, *Mater. Res. Bull.*, 2019, **112**, 331–335.

58 K. Li, H. Wang, J. Li and F. Dong, *Environ. Chem. Lett.*, 2022, **20**, 2687–2708.

59 M. H. Ashfaq, M. Imran, A. Haider, A. Shahzadi, M. Mustajab, A. Ul-Hamid, W. Nabgan, F. Medina and M. Ikram, Antimicrobial potential and rhodamine B dye degradation using graphitic carbon nitride and polyvinylpyrrolidone doped bismuth tungstate supported with in silico molecular docking studies, *Sci. Rep.*, 2023, **13**(1), 17847, DOI: **10.1038/s41598-023-44799-9**.

60 W. Zeng, M. Gao, K. Liu, C. Li, N. Cao, X. Zhao, J. Feng, Y. Ren and T. Wei, Boosting charge separation and surface defects for superb photocatalytic activity of magnesium oxide/graphene nanosheets, *Appl. Surf. Sci.*, 2021, **535**, 147658, DOI: **10.1016/j.apsusc.2020.147658**.

61 H. Kwang Benno Park, P. Kumar, I. Kebaili, I. Boukhris, Y. Hwan Joo, T. Hyun Sung and A. Kumar, Optimization and modelling of magnesium oxide (MgO) photocatalytic degradation of binary dyes using response surface methodology, *Sci. Rep.*, 2024, **14**(1), 9412, DOI: **10.1038/s41598-024-56797-6**.

62 M. Shabil Sha, H. Anwar, F. N. Musthafa, H. Al-Lohedan, S. Alfarwati, J. R. Rajabathar, J. Khalid Alahmad, J. J. Cabibihan, M. Karnan and K. Kumar Sadasivuni, Photocatalytic degradation of organic dyes using reduced graphene oxide (rGO), *Sci. Rep.*, 2024, **14**(1), 3608, DOI: **10.1038/s41598-024-53626-8**.

63 M. Krishnasamy, R. Rajendran, S. Vignesh, P. Arumugam, B. Diravidamani, M. Shkir and H. Algarni, Facile synthesis of efficient MoS$_2$-coupled graphitic carbon nitride Z-scheme heterojunction nanocomposites: photocatalytic removal of methylene blue dye under solar light irradiation, *Environ. Sci. Pollut. Res.*, 2024, **31**(34), 46513–46525, DOI: **10.1007/s11356-023-26418-2**.

28080 | *Phys. Chem. Chem. Phys.*, 2024, **26**, 28064–28081

This journal is © the Owner Societies 2024

64 S. Gupta, S. K. Ben and V. Chandra, Enhanced degradation of crystal violet dye under solar light by zirconium phosphate-decorated graphitic carbon nitride, *Res. Chem. Intermed.*, 2024, **50**(8), 3523, DOI: 10.1007/s11164-024-05307-4.

65 S. Gunalan, R. Sivaraj and V. Rajendran, Green synthesized ZnO nanoparticles against bacterial and fungal pathogens, *Prog. Nat. Sci.: Mater. Int.*, 2012, **22**, 693–700.

66 M. V. Carević, T. D. Vulić, Z. V. Šaponjić, Z. D. Mojović, N. D. Abazović and M. I. Čomor, Carbon nitride impregnated non-woven jute post-industrial waste in photocatalytic degradation of textile dyes, *Cellulose*, 2024, **31**(8), 1–16, DOI: 10.1007/s10570-024-05908-7.

67 S. Chahal, N. Rani, A. Kumar and P. Kumar, Electronic structure and photocatalytic activity of samarium doped cerium oxide nanoparticles for hazardous rose bengal dye degradation, *Vacuum*, 2020, **172**, 109075, DOI: 10.1016/j.vacuum.2019.109075.

68 J. Wu, Y. Zhang, J. Zhou, K. Wang, Y. Z. Zheng and X. Tao, Uniformly assembling n-type metal oxide nanostructures (TiO$_2$ nanoparticles and SnO$_2$ nanowires) onto P doped g-C$_3$N$_4$ nanosheets for efficient photocatalytic water splitting, *Appl. Catal., B*, 2020, **278**, 119301, DOI: 10.1016/j.apcatb.2020.119301.

69 D. Rattan Paul and S. P. Nehra, Graphitic carbon nitride: a sustainable photocatalyst for organic pollutant degradation and antibacterial applications, *Environ. Sci. Pollut. Res.*, 2021, **28**, 3888–3896.

70 L. Ge, Y. Yue, W. Wang, F. Tan, S. Zhang, X. Wang, X. Qiao and P. K. Wong, Efficient degradation of tetracycline in wide pH range using MgNCN/MgO nanocomposites as novel H$_2$O$_2$ activator, *Water Res.*, 2021, 117149, DOI: 10.1016/j.watres.2021.117149.

71 L. Dai, R. Liu, L. Q. Hu and C. L. Si, Simple and green fabrication of AgCl/Ag-cellulose paper with antibacterial and photocatalytic activity, *Carbohydr. Polym.*, 2017, **174**, 450–455.

72 N. Abdel-Raouf, N. M. Al-Enazi and I. B. M. Ibraheem, Green biosynthesis of gold nanoparticles using Galaxaura elongata and characterization of their antibacterial activity, *Arabian J. Chem.*, 2017, **10**, S3029–S3039.

This journal is © the Owner Societies 2024

Phys. Chem. Chem. Phys., 2024, **26**, 28064–28081 | **28081**